

## ARTICLE

Received 29 Aug 2014 | Accepted 3 Dec 2014 | Published 13 Jan 2015

DOI: 10.1038/ncomms7028

OPEN

# Engineering two-dimensional superconductivity and Rashba spin-orbit coupling in $\text{LaAlO}_3/\text{SrTiO}_3$ quantum wells by selective orbital occupancy

Gervasi Herranz<sup>1</sup>, Gyanendra Singh<sup>2</sup>, Nicolas Bergeal<sup>2</sup>, Alexis Jouan<sup>2</sup>, Jérôme Lesueur<sup>2</sup>, Jaume Gázquez<sup>1</sup>, María Varela<sup>3,4</sup>, Mateusz Scigaj<sup>1,5</sup>, Nico Dix<sup>1</sup>, Florencio Sánchez<sup>1</sup> & Josep Fontcuberta<sup>1</sup>

The discovery of two-dimensional electron gases (2DEGs) at oxide interfaces—involving electrons in narrow *d*-bands—has broken new ground, enabling the access to correlated states that are unreachable in conventional semiconductors based on *s*- and *p*- electrons.

There is a growing consensus that emerging properties at these novel quantum wells—such as 2D superconductivity and magnetism—are intimately connected to specific orbital symmetries in the 2DEG sub-band structure. Here we show that crystal orientation allows selective orbital occupancy, disclosing unprecedented ways to tailor the 2DEG properties. By carrying out electrostatic gating experiments in  $\text{LaAlO}_3/\text{SrTiO}_3$  wells of different crystal orientations, we show that the spatial extension and anisotropy of the 2D superconductivity and the Rashba spin-orbit field can be largely modulated by controlling the 2DEG sub-band filling. Such an orientational tuning expands the possibilities for electronic engineering of 2DEGs at  $\text{LaAlO}_3/\text{SrTiO}_3$  interfaces.

<sup>1</sup>Institut de Ciència de Materials de Barcelona (ICMAB-CSIC), Campus de la UAB, 08193 Bellaterra, Catalonia, Spain. <sup>2</sup>LPEM-UMR8213/CNRS-ESPCI ParisTech-UPMC, PSL University, 10 rue Vauquelin, 75005 Paris, France. <sup>3</sup>Materials Science & Technology Division, Oak Ridge National Laboratory, Oak Ridge, Tennessee 37831, USA. <sup>4</sup>GFMC, Department de Física Aplicada III & Instituto Pluridisciplinar, Universidad Complutense de Madrid, 28040 Madrid, Spain. <sup>5</sup>Departament de Física, Universitat Autònoma de Barcelona, E-08193 Bellaterra, Barcelona, Catalonia, Spain. Correspondence and requests for materials should be addressed to G.H. (email: gherranz@icmab.cat).

The confinement of electron orbitals over small scales provides a pathway to tailor the electronic properties of a quantum system. Restricting the motion of electrons within planes of **different crystal orientation** affords additional routes to reorganize the electronic band structure. Such strategies have been used to **engineer the electronic and optical properties of II–VI and III–V semiconductor quantum wells, where *s*- and *p*- orbitals are involved**<sup>1–3</sup>. Yet, two-dimensional (2D) electron gases (2DEGs), comprising *d*-electrons instead of *s* or *p*, have come into the limelight over about the last 10 years<sup>4–11</sup>, opening novel perspectives that are inaccessible for more traditional materials. In particular, the narrow bandwidth of *d*-states in transition metal oxide quantum wells promote correlated states—for example, magnetism and superconductivity—that are unseen in conventional semiconductors. Interestingly, the extreme confinement, over just a few unit cells, enables full electrostatic control of correlated 2DEG states, allowing access to new physics and paving the way to new device concepts. Particularly, these 2D electron systems have been found to be superconductive<sup>7,12–14</sup>, with 2D superconductivity largely modulated by electric gates<sup>15,16</sup>. The 2D character of the superconductivity has led to phenomena not observed in the 3D regime, such as magnetic enhancement of superconductivity<sup>17</sup>, violation of the paramagnetic Pauli limit for the upper critical fields<sup>18</sup>, quantum phase transitions<sup>19</sup> or multiple quantum criticality<sup>20</sup>. The intricacy of all these complex phases and the evidence of the role of electron correlations have often prompted the use of the concept of electron liquids to designate these electron systems<sup>21</sup>.

The interface between LaAlO<sub>3</sub> and SrTiO<sub>3</sub> is the oxide quantum well par excellence. Initially, the research on LaAlO<sub>3</sub>/SrTiO<sub>3</sub> quantum wells was restricted to the (001)-plane of the perovskite unit cell<sup>4,14,15</sup>. Remarkably, recent investigations have uncovered that interface conductivity also appears along other directions, such as (110) (refs. 22,23) and (111) (ref. 22). The selective confinement of electrons within planes of different crystal orientation expands vigorously the possibility of fine-tuning the 2DEG sub-band hierarchy and, thereof, the physical properties. Along this line, we have recently demonstrated that crystal symmetry is an extra degree of freedom to realize different 2DEG band reconstructions at the LaAlO<sub>3</sub>/SrTiO<sub>3</sub> interface, by imposing distinctive orbital hierarchies on (001)- and (110)-oriented quantum wells and enabling the selective occupancy of states of different symmetry<sup>24</sup>. More specifically, we have uncovered that the degeneracy within the *t*<sub>2g</sub> sub-band—which forms the backbone of the 2DEG structure in LaAlO<sub>3</sub>/SrTiO<sub>3</sub> wells—is broken in reversed ways depending on the crystal orientation: for (001)-oriented 2DEGs the *d*<sub>xy</sub> orbitals have the lowest energy, while along (110) the bottommost levels have instead a *d*<sub>xz</sub>/*d*<sub>yz</sub> character<sup>24</sup>. Recent experiments on uncapped (110) SrTiO<sub>3</sub> surfaces also found the same hierarchy<sup>25</sup>. This orbital reconfiguration provides an excellent playground to test the link between orbital symmetry and complex correlated states, provided that we understand exactly the implications that such 2DEG band engineering has for the physical properties of the quantum wells.

In this work, we present evidence that the selection of the orbital symmetries in the 2DEG sub-band structure triggers some nontrivial and extensive modifications of the electronic properties of quantum wells at the LaAlO<sub>3</sub>/SrTiO<sub>3</sub> interface. First, we demonstrate that **the orbital reconfiguration implies a modulation of 2DEG spatial extension and, as a result, the anisotropy of the 2D superconductivity** is largely affected by crystal orientation. Second, we show that the effects of sub-band engineering are **influential on the spin–orbit coupling and the concomitant Rashba effect, opening new pathways to tune the spin-dependent transport in LaAlO<sub>3</sub>/SrTiO<sub>3</sub> quantum wells**. These findings open

fresh perspectives to understand the fundamental connection between orbital symmetry and the electronic phases at LaAlO<sub>3</sub>/SrTiO<sub>3</sub> interfaces.

## Results

**Structural characterization.** The samples analysed here were obtained by pulsed laser deposition of LaAlO<sub>3</sub> thin films on TiO<sub>2</sub>-terminated (001)-SrTiO<sub>3</sub> substrates (LaAlO<sub>3</sub> thickness *t* = 10 monolayers (MLs), corresponding to *t* ~ 3.8 nm) as well as on thermally treated (110)-oriented SrTiO<sub>3</sub> substrates (*t* = 7–14 MLs, *t* ~ 1.9–3.8 nm), see details in Methods and (refs 22,26,27). We carried out cross-sectional scanning transmission electron microscopy (STEM) in the high-angle annular dark field (HAADF) imaging mode, in which, to a good approximation, the intensity of an atomic column is proportional to the square of the atomic number (*Z*), so elements can be deduced by tracking column intensities<sup>28</sup>. Brighter atomic columns correspond to the heavier elements, La and Sr, whereas fainter columns correspond to Ti and Al. Atomic-scale structural characterization shows a coherent and epitaxial growth of both heterostructures and atomically flat interfaces—Fig. 1a,b for (001) and (110), respectively— Besides, regarding the (110)-oriented sample, along the [001] zone axis the (110) ionic stacking across the interface can be readily appreciated, see Fig. 1b. Therefore, in spite of the higher surface energies of (110)-planes with respect to (001), the STEM-HAADF study rules out altogether the formation of (100) microfacets at the (110)-interface<sup>23,29,30</sup>.

## Spatial extension and anisotropy of 2D superconductivity.

We discuss first the implications of band reconstruction on the 2DEG superconductivity. In line with previous reports on (001) (refs 14,15,19), we show that the (110)-interface is also superconductive and has a 2D character. Yet, we uncover that the anisotropy of the 2D superconductive state is considerably larger for (001) than for (110). Such a conclusion is readily apparent from the sheet resistance curves measured under the magnetic fields applied in-plane (Fig. 2a,b). It is known that as the 2D limit is approached, increasingly higher in-plane fields are required to suppress the superconductivity, since vortex entry is impeded by the low dimensionality<sup>13</sup>. Therefore, higher in-plane critical fields imply stronger anisotropy. Inspection of Fig. 2a,b shows that the (001) interface requires much higher in-plane fields ( $\mu_0 H_{c2,\parallel} \approx 2,200$  mT) than the (110) interface ( $\mu_0 H_{c2,\parallel} \approx 1,000$  mT) to induce the transition to the normal state. We conclude, thus, that the 2D anisotropy is larger for (001) than for (110), anticipating a smaller spatial extension of the quantum well along (001).

For a quantitative estimation of both the superconductive layer thickness *d* and the in-plane superconductive coherence length  $\xi$ , we carried out an analysis based on the Landau–Ginzburg formalism<sup>31</sup>. For that purpose, the out-of-plane  $\mu_0 H_{c2,\perp}$  and in-plane  $\mu_0 H_{c2,\parallel}$  critical fields were determined by defining quantitative criteria for the field-induced transitions. Thus, a drop resistance of 90% from the normal resistance state at *T* = 400 mK was established to ascertain the evolution of the transition temperature *T*<sub>C</sub>. We consider first the (110) sample with LaAlO<sub>3</sub> thickness *t* = 14 MLs. The out-of-plane critical field, extrapolated to *T* = 0 K, was  $\mu_0 H_{c2,\perp} \approx 160$  mT (Supplementary Fig. 1), leading to an in-plane coherence length  $\xi = \sqrt{\frac{\Phi_0}{2\pi\mu_0 H_{c2,\perp}}} \approx 44$  nm ( $\Phi_0$  is the flux quantum)<sup>31</sup>. In addition, from the in-plane critical field  $\mu_0 H_{c2,\parallel} \approx 1,000$  mT we could estimate the superconductive thickness  $d = \frac{\Phi_0 \sqrt{3}}{\pi\mu_0 H_{c2,\parallel} \xi} \approx 24$  nm. Since the coherence length is well above the superconductive thickness (*d* <  $\xi$ ), the superconductivity is shown to be 2D. Applying the

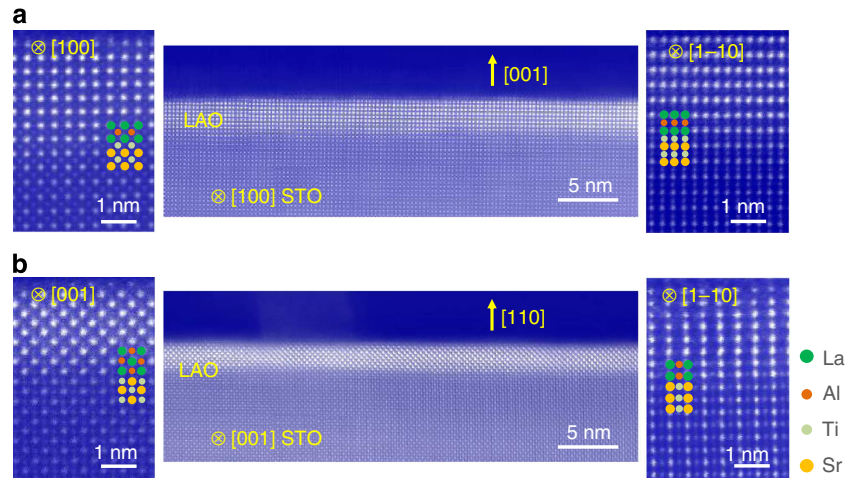


**Figure 1 | Atomic-resolution STEM characterization.** (a) HAADF-STEM images of the  $\text{LaAlO}_3/\text{SrTiO}_3$  (001) interface. The left and right panels are magnified views of the interface observed from [100] and [1-10] zone axes, respectively. (b) HAADF-STEM images of the  $\text{LaAlO}_3/\text{SrTiO}_3$  (110) interface. Left and right panels are magnified views of the interface observed from [001] and [1-10] directions, respectively. Both  $\text{LaAlO}_3$  layers are continuous within the analysed region (of the order of  $1\mu\text{m}$ ). The images in the central panels **a** and **b** have been Fourier filtered to reduce background noise. The positions of La and Sr are indicated by green and orange circles, whereas Al and Ti are shown in red and light green. Note that for both orientations the interfaces are atomically flat and that the (110) interface does not show any local (100) microfacet.

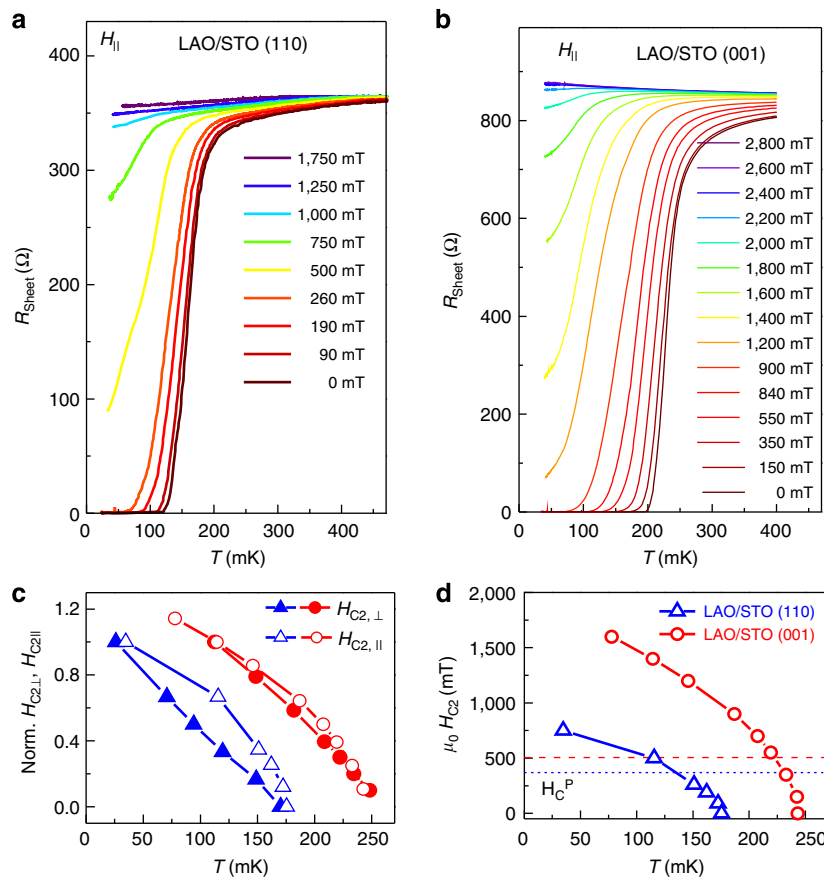


**Figure 2 | Anisotropy of the 2D superconductivity at the (001) and (110) interfaces.** Sheet resistance of (a) the (110)-interface with  $t = 14$  MLs and (b) the (001)-interface with  $t = 10$  MLs, under magnetic fields applied parallel to the interface. The field values are indicated in the panels. Panel (c) shows the temperature dependence of out-of-plane  $\mu_0 H_{c2,\perp}$  and in-plane  $\mu_0 H_{c2,\parallel}$  critical fields of (001)—red circles—and (110)—blue triangles—interfaces, corroborating the 2D character of the superconductivity for both orientations. (d) The upper critical fields are displayed as a function of the temperature for both the orientations (field in-plane). The dotted and dashed straight lines indicate the Pauli-limited critical fields  $\mu_0 H_c^p$ . The observation of higher critical fields for the (001) interface is consistent with the larger anisotropy of the 2DEG superconductivity and stronger spatial confinement for (001).

same protocol analysis to the other (110)-interfaces in this study, with thickness in the range  $t = 7\text{--}10$  MLs (Supplementary Fig. 2), we find that always the in-plane coherence length ( $\xi \approx 40\text{--}75$  nm) is significantly larger than the superconductive thickness ( $d \approx 24\text{--}30$  nm), thus confirming the 2D character of the superconductivity at the (110) interface. This is also corroborated by the analysis of the temperature dependence of the resistance, showing that the transition to the superconductivity at (110) interfaces belongs to the Berezinskii–Kosterlitz–Thouless (BKT) universality class<sup>32–34</sup> (Supplementary Fig. 3). In addition, the out-of-plane and in-plane critical fields follow the temperature dependence expected for 2D superconductors (Fig. 2c), that is,  $\mu_0 H_{c2,\perp} = \frac{\Phi_0}{2\pi\xi^2} (1 - T/T_C)$  and  $\mu_0 H_{c2,\parallel} = \frac{\Phi_0\sqrt{12}}{2\pi\xi d} (1 - T/T_C)^{1/2}$ , respectively<sup>13</sup>.

We applied also the Landau–Ginzburg analysis to a (001)  $\text{LaAlO}_3/\text{SrTiO}_3$  sample using the same growth conditions as those used for the (110)-oriented samples. The analysis of the experimental data concludes that the coherence length is  $\xi \approx 40$  nm and the superconducting thickness is  $d \approx 13$  nm, in close agreement with the values previously reported<sup>14,35</sup>. We, thus, demonstrate in a quantitative manner that the spatial extension of superconductive (110) interfaces ( $d \approx 24\text{--}30$  nm) is considerably larger than the one usually reported for (001) interfaces ( $d \approx 10\text{--}13$  nm) (refs 14,35).

The wider spatial extent of the (110)-2D state is also inferred from the analysis of the Pauli paramagnetic limit of the upper critical fields. For high-enough magnetic fields, the paramagnetic susceptibility induces a parallel alignment of the Cooper pair spins that eventually breaks them apart, giving a higher bound for the upper critical fields<sup>18,36</sup>. This value can be assessed as  $\mu_0 H_c^p \approx 1.76 k_B T_C / \sqrt{2} \mu_B$ , where  $k_B$  is the Boltzmann's constant and  $\mu_B$  is the Bohr magneton (assuming a  $g$  factor of 2)<sup>18,36</sup>. Although this upper bound is generally fulfilled, it is violated in some cases. One example is the case of ultrathin  $\text{SrTiO}_3$  2D superconducting layers for which the values of  $\mu_0 H_{c2,\parallel}$  were found to exceed largely the Pauli limit. This was explained by the large intrinsic spin–orbit coupling at interfaces, which becomes a prominent energy scale as the thickness is reduced<sup>18</sup>. The correlation between the spatial confinement and the anisotropy of the 2D superconductivity is also borne out in the (001) and (110)  $\text{LaAlO}_3/\text{SrTiO}_3$  interfaces. Figure 2d summarizes this observation: the upper critical fields  $\mu_0 H_{c2,\parallel}$  measured in (001) interfaces are significantly higher than those measured in (110) samples at any temperature. As a matter of fact, for the (001) interface the Pauli limit is already violated at temperatures below  $T \leq 220$  mK, close to  $T_C$ . Instead, the Pauli limit is only surpassed at temperatures  $T \leq 110$  mK for the (110) interface, further away from the transition (Fig. 2d). Again, this is an indication of stronger 2DEG confinement at the (001) interface.

**Electrostatic modulation of 2D superconductivity.** The different 2DEG spatial extent has also consequences on the electrostatic modulation of the superconductivity. We performed electrostatic gating experiments in (001)- and (110)-oriented samples that were contacted by top and backgate electrodes and electric fields were applied in the range of  $V_g = \pm 400$  V (Fig. 3). Positive/negative voltages correspond to the accumulation/depletion of electrons at the interface, respectively. Hall and capacitance experiments allowed us to obtain the sheet carrier density modulation as a function of the voltage  $V_g$  for both the film orientations. The curves of carrier density that we extract from Hall measurements exhibit a reduction of  $n_{\text{Hall}}$  for positive  $V_g$  (Fig. 3f). Such a feature is the hallmark of multiband conduction, in which high- and low-mobility carriers participate in the transport in the regime of accumulation, whereas only one type of carrier is

relevant in the regime of depletion ( $V_g \ll 0$ ) (ref. 16). The total carrier density  $n_s$ , comprising both heavy and light electron bands, can be obtained by experiments that measure the capacitance between the backgate and the 2DEG. In this case, the value of  $n_s$  is extracted by integration over the voltage range  $n_s(V_g) = n_s(V_g = -V) + \frac{1}{eA} \int_{-V}^V C(V) dV$ , where  $A$  is the area of the capacitor. Note that, in agreement with the two-carrier scenario, only one band is involved in transport at negative  $V_g$  and  $n_s$  is superimposed to  $n_{\text{Hall}}$  within this range of applied voltages (Fig. 3f). Instead, in the regime of accumulation,  $V_g > 0$ , two bands are involved and  $n_s$  and  $n_{\text{Hall}}$  differ significantly<sup>16,37</sup>.

Figure 3e summarizes the results of the electrostatic gating experiments, where the superconducting transition temperature  $T_C$  and the resistance  $R_{\text{sheet}}$  at the normal state are plotted as a function of the gate voltage  $V_g$ . We see that the carrier density is largely modulated for both orientations, with variations  $\Delta n_s = 0.2 - 0.8 \times 10^{14} \text{ cm}^{-2}$  and  $\Delta n_s = 0.4 - 1.6 \times 10^{14} \text{ cm}^{-2}$  for (001) and (110) interfaces, respectively. However, despite similar modulations of the carrier density for both orientations, their effects on the superconductivity are dramatically different depending on the crystal orientation. More specifically, the superconductivity of the (001)-interface could be suppressed for a range of applied fields (Fig. 3a), in agreement with previous reports<sup>15</sup>. At the (001) interface the  $T_C(V_g)$  curve exhibits a dome-like shape (Fig. 3e), indicating that superconductivity is suppressed at fields above  $V_g \approx +200$  V and below  $V_g \approx -50$  V. Instead, for (110) interfaces the superconducting state is never switched off by electric fields (Fig. 3b) and the transition temperature is modulated by at most about 50% (Fig. 3e). The much larger tunability of (001) interfaces with respect to (110) is again consistent with the narrower extension of 2DEGs at (001) wells.

**Modulation of the Rashba spin–orbit field.** Previous works have demonstrated that **there is a strong spin–orbit field that stems from a Rashba-type interaction at the  $\text{LaAlO}_3/\text{SrTiO}_3$  interface<sup>38,39</sup>. As a result, an effective magnetic field  $B_{\text{SO}}$  is felt by electrons moving relativistically under the influence of the interface intensive electric fields  $E_0 = -\nabla V(r)$ . Remarkably, the intensity of  $B_{\text{SO}}$  is directly related to electron hopping between  $t_{2g}$  orbitals that, although forbidden in the unperturbed system away from interfaces, are however allowed in the presence of the field  $E_0$  (ref. 40). In particular,  $E_0$  induces a polarization of the atomic orbitals, which break their symmetry and, as a consequence, allows a hybridization within the  $t_{2g}$  manifold in the metal–oxygen network that contributes to  $B_{\text{SO}}$  (refs 40,41). Because of the different 2DEG band structure along (001) or (110), the spin–orbit field  $B_{\text{SO}}$  is expected to have a strong orientational dependence.**

To probe the effects of orientational reconstruction on the spin–orbit term  $B_{\text{SO}}$ , we analysed the field dependence of the magnetoconductance at the normal state recorded at a temperature  $T = 3.3$  K under applied electric fields (Fig. 4a,b). The experimental data were fitted to the expression<sup>38,42</sup>

$$\frac{\Delta\sigma(B)}{G_0} = -\Psi\left(\frac{1}{2} + \frac{B_{\text{tr}}}{B}\right) + \frac{3}{2}\Psi\left(\frac{1}{2} + \frac{B_{\phi} + B_{\text{SO}}}{B}\right) - \frac{1}{2}\Psi\left(\frac{1}{2} + \frac{B_{\phi}}{B}\right) - \left[\ln\left(\frac{B_{\phi} + B_{\text{SO}}}{B_{\text{tr}}}\right) + \frac{1}{2}\ln\left(\frac{B_{\phi} + B_{\text{SO}}}{B_{\phi}}\right)\right] - A_K \frac{\sigma(0)}{G_0} \frac{B^2}{1 + CB^2} \quad (1)$$

that describes the change of conductivity with field  $\Delta\sigma(B)$  normalized by the quantum of conductance  $G_0 = e^2/\pi h$  (refs 38,42,43). In equation (1), quantum corrections to the conductance in the 2D limit are described by the four first terms, where  $\Psi(x)$  is the digamma function, and  $B_{\text{tr}}$ ,  $B_{\phi}$  and  $B_{\text{SO}}$  are the



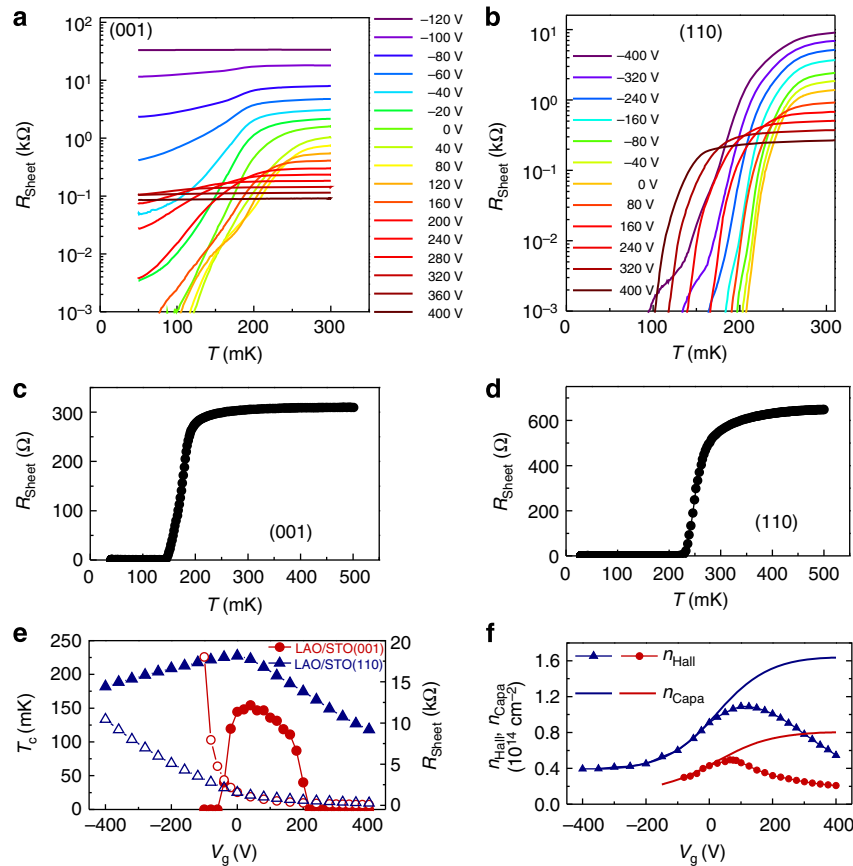


**Figure 3 | Electrostatic modulation of the 2D-superconductivity at the (001) and (110) interfaces.** Temperature dependence of the resistance as a function of gate voltage for (a) (001)—and (b) (110)-oriented LaAlO<sub>3</sub>/SrTiO<sub>3</sub> interfaces, respectively. In panels (c) and (d) we show the superconducting transitions in linear scale, for zero applied voltage, for (001) and (110) interfaces, respectively. (e) Superconducting  $T_c$  (filled symbols) and sheet resistance (open symbols) of (001)—and (110)-interfaces plotted against the gate voltage. (f) Hall carrier density of (001)- (circles) and (110)- (triangles) interfaces. Solid lines correspond to the carrier density obtained from the analysis of the capacitance.

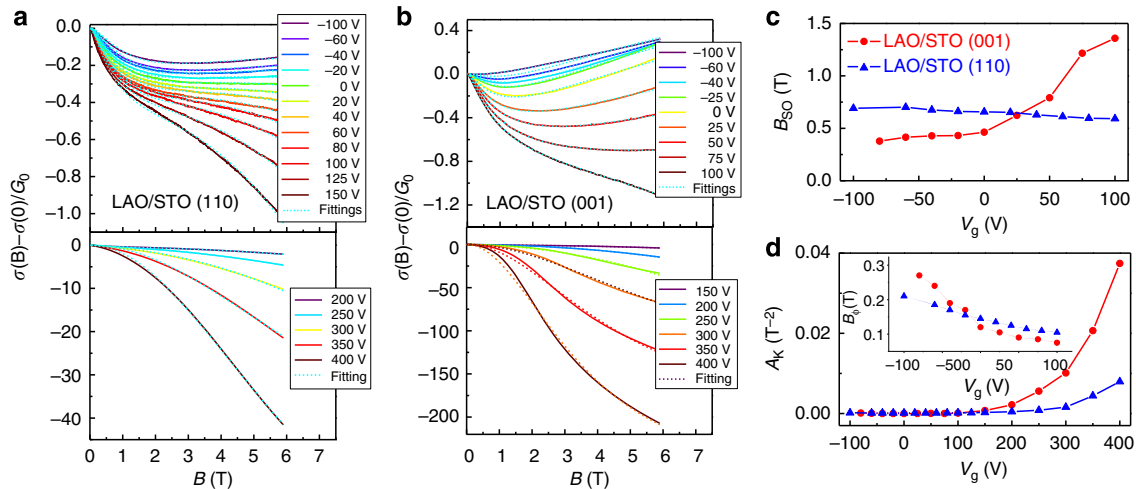


**Figure 4 | Analysis of the spin-orbit coupling at the (001) and (110) interfaces.** The field-dependent magnetoconductance  $\Delta\sigma(B)$  normalized by the quantum of conductance  $G_0$  was measured under different gate voltages  $V_g$ . Data measured at  $T = 3.3$  K are shown for the (a) (110) and (b) (001) interfaces. Dashed lines are the fittings to equation (1) and the values of the applied voltage are indicated in the panels. The dependence of the spin-orbit term  $B_{SO}$  on the gate voltage  $V_g$  is plotted (c). The Kohler  $A_K$  and inelastic  $B_\phi$  terms obtained from fittings to equation (1) are plotted in (d) and inset, respectively.

effective fields related to the elastic, inelastic and spin-orbit scattering terms, respectively<sup>43</sup>. Finally, the last term in equation 1, involving the parameters  $A_K$  and  $C$ , is the Kohler

term that gives an account of orbital magnetoresistance. Fittings of the experimental data to equation (1) were excellent, as shown in Fig. 4a,b for both orientations and for different electric fields.

The parameters  $B_{SO}$ ,  $A_K$  and  $B_\phi$  extracted from these fittings are shown in Fig. 4c,d. It turns out that the Kohler term  $A_K$  became rather large at positive fields  $V_g > +100$  V (Fig. 4d), making difficult a precise evaluation of the spin–orbit term in the regime of strong electron accumulation. For that reason in Fig. 4c we plotted the evolution of the term  $B_{SO}$  restricted to the range  $V_g = \pm 100$  V, where accurate values of the spin–orbit contribution can be obtained.

For the (001) sample, the values of  $B_{SO}$  that we obtained from fittings to equation (1) are in the same range as reported previously for the same orientation, with a similar asymmetric dependence of the spin–orbit field with  $V_g$  (refs 38,43). In the regime of depletion ( $V_g < 0$  V), the values of the spin–orbit field are  $B_{SO} < 0.5$  T, whereas for electron accumulation ( $V_g > 0$  V) the spin–orbit term rises up to  $B_{SO} \approx 1.5$  T. We thus observe a strong asymmetric field dependence of  $B_{SO}$  for the interfaces along (001). In contrast, the electrostatic modulation of  $B_{SO}$  is very weak along (110), and the spin–orbit field is largely unaffected by the electrostatic gating, with values restricted within a much narrower range  $B_{SO} \approx 0.6$ – $0.7$  T (Fig. 4c). In brief, our analysis demonstrates that the Rashba spin–orbit fields at the (110) interfaces are substantially different from those along (001). This observation illustrates how band engineering based on crystal symmetry can be exploited to tailor the spin-dependent transport along SrTiO<sub>3</sub>-based quantum wells<sup>44,45</sup>.

## Discussion

The different spatial extension of the quantum wells along (001) and (110) and the different behaviour of the Rashba spin–orbit fields can be elucidated on the grounds of the modulation of the 2DEG sub-band structure observed in the experiments<sup>24</sup> that, in turn, can be understood using the fundamental concepts of quantum physics of solids. When we consider the orbitals of  $t_{2g}$

electrons that are confined along (001) or (110), the quantum well entrapment of  $d_{xy}$ ,  $d_{xz}$  and  $d_{yz}$  wavefunctions produces an energy splitting between the different eigenstates that is inversely proportional to their effective masses along the confinement direction<sup>46</sup>. Figure 5 illustrates schematically the arguments that we expose in the following. Note that although the full complexity of the quantum sub-band structure<sup>47,48</sup> is ignored in this Figure—as we depict only one sub-band for each type of orbital—the essential physics is captured. More specifically, for confinement along (001),  $\pi$ -type bonding between  $d_{xy}$  states leads to small wavefunction overlapping and large effective mass, while along (110)  $\sigma$ -like bonds between  $d_{xy}$  orbitals lead to much smaller effective mass (Fig. 5a,b). Instead, the overlapping of  $d_{xz}/d_{yz}$  states has intermediate values for both the orientations. This results in a hierarchy of out-of-plane effective masses given by  $m_{xy, <001>}^* \gg (m_{xz, <001>}^*, m_{xz, <110>}^*, m_{yz, <001>}^*, m_{yz, <110>}^*) \gg m_{xy, <110>}^*$  that, in turn, yields the energy orbital landscape outlined in Fig. 5c,d, which is in agreement with the 2DEG sub-band hierarchy observed in X-ray linear dichroism experiments<sup>46,49</sup>.

As a consequence of the observed rearrangement of orbital symmetries, the spatial extension of the 2DEG must change significantly with the crystal orientation. In this respect, Fig. 5c,d plot schematically the carrier spatial distributions of  $d_{xy}$ ,  $d_{xz}$  and  $d_{yz}$  states: along (001) the first  $d_{xy}$  sub-band is expected to be at the bottom of the well, with little spatial spread; on the contrary, along (110) the  $d_{xy}$  level raises its energy above the  $d_{xz}/d_{yz}$  states, and its spatial extent is considerably larger. In addition to orbital occupancy, contributions from the anisotropic character of the dielectric constant tensor may also influence the 2DEG spatial extent. Therefore, the modulation of the orbital hierarchy described here provides a natural explanation for the distinct anisotropy of the 2D superconductivity and spatial extension for quantum wells oriented along (001) and (110).

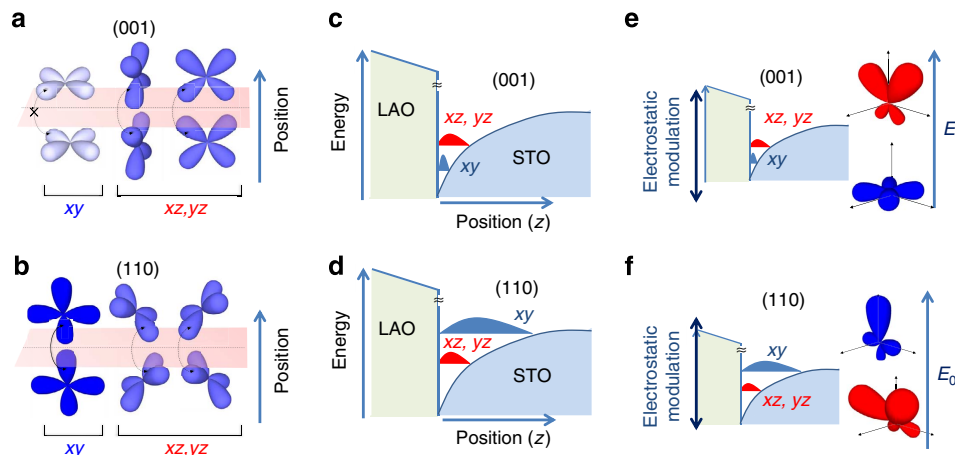


**Figure 5 | Energy landscape and orbital symmetries of 2DEGs at (001) and (110) LaAlO<sub>3</sub>/SrTiO<sub>3</sub> interfaces.** (a) Along (001), the overlapping of  $d_{xy}$  orbitals is very small, while it is moderately large for  $d_{xz}/d_{yz}$  states. (b) Along (110), the overlapping of  $d_{xy}$  orbitals is the largest. Since the effective mass along the confinement direction is inversely proportional to the orbital overlapping, the hierarchy of masses is given by  $m_{xy, <001>}^* \gg (m_{xz, <001>}^*, m_{xz, <110>}^*, m_{yz, <001>}^*, m_{yz, <110>}^*) \gg m_{xy, <110>}^*$ . The rules of quantum physics in solids dictate the energy landscape in the quantum wells: (c) Orbitals with symmetry  $d_{xy}$  lie at the bottom of (001) quantum wells, while  $d_{xz}/d_{yz}$  are higher in energy; (d) Along (110), the  $d_{xz}/d_{yz}$  states have lower energy and the  $d_{xy}$  levels are at the top. The different energy hierarchy of orbitals determines a larger spatial extension for 2DEGs along (110) as compared with (001). (e) Sketches how the  $d_{xy}$  and  $d_{xz}/d_{yz}$  orbitals are distorted by the inversion symmetry breaking field  $E_0$  at the interface. Along (001),  $d_{xy}$  states have a small projection along the out-of-plane direction and they are weakly polarized by  $E_0$ , whereas  $d_{xz}/d_{yz}$  states project along the direction of confinement and are largely polarized. (f) Instead, along (110), both kinds of orbitals are affected similarly by the interface fields. Within the range of applied fields, the electrostatic modulation has dissimilar effects on the spin–orbit fields  $B_{SO}$ . Along (001), only  $d_{xy}$  orbitals are filled at  $V_g < 0$ , whereas at  $V_g > 0$  the  $d_{xz}/d_{yz}$  states are progressively occupied. Thus, at low electrostatic doping,  $B_{SO}$  is smaller because of the relatively small atomic orbital polarization of  $d_{xy}$  states, whereas the population of  $d_{xz}/d_{yz}$  orbitals at positive  $V_g$  increases significantly  $B_{SO}$ . Instead, along (110) the dependence of  $B_{SO}$  on the applied fields is weak, because all  $t_{2g}$  orbitals are expected to undergo polarizations of similar strength.

By the same token, the redistribution of the orbital sub-band hierarchy also explains the distinctive dependence of the Rashba spin-orbit fields on the orientation. As mentioned above, the interface electric field  $E_0$  induces a polarization of the atomic orbitals that breaks their symmetry along the direction of the quantum well. This enables new covalent channels within the  $t_{2g}$  manifold and the oxygen network that contributes to  $B_{SO}$  (refs 40,41). The key point is to recognize that orbitals with large projections over the normal to the interface are those more sensitive to the inversion symmetry breaking fields  $E_0$ , giving larger Rashba effects<sup>40,41</sup>. Such atomic orbital polarization is graphically depicted in Fig. 5e in the form of spatially distorted orbitals.

In the light of these observations, the asymmetric modulation of  $B_{SO}$  with field along (001), Fig. 4c, can be explained because  $d_{xy}$  orbitals are weakly polarized due to their minimal projection along the confinement direction, while  $d_{xz}/d_{yz}$  states have much stronger spatial asymmetry (Fig. 5e). As a result of the 2DEG sub-band hierarchy along (001), the electrostatic modulation of orbital occupancy is anticipated to give a significant variation of  $B_{SO}$  as a function of the orbital occupancy: at  $V_g < 0$  V only  $d_{xy}$  orbitals are populated; the orbital polarization is weak (Fig. 5e) and  $B_{SO}$  is relatively small. In contrast, as we enter the regime of accumulation and  $d_{xz}/d_{yz}$  bands start to be filled, the spin-orbit term begins to increase significantly, in agreement with the significantly larger orbital polarization of these orbitals.

The situation is radically different for the (110) interface. Now, the electrostatic modulation of  $B_{SO}$  is very weak and the spin-orbit field is largely unaffected by the electrostatic gating. This behaviour, which may seem surprising in the light of the modulation of carrier density with electrostatic gating (Fig. 4d), can be well understood on the grounds of the similar atomic orbital polarizations of  $d_{xy}$  and  $d_{xz}/d_{yz}$  orbitals along (110), Fig. 5e. Indeed, along (110), all  $t_{2g}$  orbitals are expected to undergo similarly strong polarizations (Fig. 5e) and, therefore, the spin-orbit field  $B_{SO}$  is expected to have a rather weak dependence on the applied field, as confirmed by the experiments.

In summary, we have shown that the orbital reconstruction that occurs for  $\text{LaAlO}_3/\text{SrTiO}_3$  quantum wells confined along two different directions, (001) and (110) has a deep impact on the physical properties of these 2DEGs. We claim that the different energy landscapes and hierarchy of orbital symmetries are behind the observed differences in the 2DEG spatial extensions and spin-orbit fields. The analysis of the 2D superconductivity is consistent with 2DEGs extending spatially over (110) at larger distances than at (001) interfaces. At the same time, electrostatic gating experiments have provided relevant clues to understand the distinctive spatial distribution of  $t_{2g}$  states with respect to the interface that results from the modified energy sub-band hierarchy and the renormalization of the associated effective band masses. Our work shows that crystal symmetry is an extra degree of freedom to realize different 2DEG band reconstructions at the  $\text{LaAlO}_3/\text{SrTiO}_3$  interface, thus allowing a selective occupancy of states of different symmetry. Such new perspective for 2DEG band engineering is very alluring, as it opens new research fields to extend our current understanding of the link between orbital symmetry and magnetism and superconductivity at  $\text{LaAlO}_3/\text{SrTiO}_3$  quantum wells.

## Methods

**Sample preparation.** For the growth of (110)-oriented samples, the  $\text{SrTiO}_3$  substrates were treated in a dedicated furnace at 1,100 °C for 2 h under ambient conditions<sup>26,27</sup>. Samples with (001) orientation were grown on  $\text{TiO}_2$ -terminated  $\text{SrTiO}_3$  substrates. The  $\text{TiO}_2$  termination of the  $\text{SrTiO}_3$ (001) single crystals was obtained by chemical treatment followed by thermal annealing<sup>50,51</sup>.  $\text{LaAlO}_3$  thin films were grown by pulsed laser deposition ( $\lambda = 248$  nm) monitored by high pressure reflection high-energy electron diffraction. The substrates were heated

from room temperature to deposition temperature (850 °C) in an oxygen partial pressure  $P_{\text{O}_2} = 0.1$  mbar. During deposition, the  $\text{LaAlO}_3$  was grown under a pressure  $P_{\text{O}_2} = 10^{-4}$  mbar and 1-Hz repetition rate, with laser pulse energy of around 26 mJ. Films with thickness 7, 8, 10 and 14 MLs were prepared on (110) substrates, whereas the (001)-oriented sample had a  $\text{LaAlO}_3$  thickness of 10 MLs. At the end of the deposition, samples were cooled down in an oxygen rich atmosphere to minimize the formation of oxygen vacancies that could lead to extrinsic mechanisms of conduction. More specifically, the samples were cooled from  $T = 850$  to 750 °C under a pressure  $P_{\text{O}_2} = 0.3$  mbar and under  $P_{\text{O}_2} = 200$  mbar from  $T = 750$  °C down to room temperature, including a dwell time of 1 h at 600 °C.

**Magnetotransport.** The electrical characterization was performed by using six-contact arrangement in Hall geometry, from which the sheet resistance, sheet carrier density and electron mobility were extracted as a function of temperature and gate voltage. The current was injected along the in-plane (001) direction in (110)-interfaces. The  $\text{LaAlO}_3/\text{SrTiO}_3$  interface was contacted via ultrasonic wire bonder with Al wires. Measurements at temperatures below 1.8 K were measured in a dilution cryostat by applying 50 nA AC current of frequency 13.67 Hz. For the estimation of critical field, the magnetic field was applied parallel and perpendicular to the sample plane with sweep rates of  $1.6 \text{ mT s}^{-1}$ . For the measurement of the parallel critical magnetic field of the 110 samples, the field was applied in the same direction than the current, that is, along the in-plane (001). Electric fields were applied using voltage source. No leakage current ( $< 5$  nA) was detected up to largest applied voltages  $\pm 400$  V.

**Transmission electron microscopy.** STEM-HAADF images were acquired with a NION UltraSTEM, equipped with a 5th order NION aberration corrector and operated at 200 kV, and in a FEI Titan (60–300 kV) STEM operated at 300 kV, equipped with a probe Cs corrector from CEOS, a monochromator and a high-brightness field-emission gun (X-FEG). HAADF signals for the samples were collected from the detector inner-angles of  $\sim 86$  and  $\sim 60$  mrad for the NION and FEI Titan microscopes, respectively. Specimens for STEM were prepared by conventional methods, by grinding, dimpling and argon ion milling.

## References

- Park, S.-H. Crystal orientation effects on electronic properties of wurtzite  $\text{InGaN}/\text{GaN}$  quantum wells. *J. Appl. Phys.* **91**, 9904–9908 (2002).
- Feneberg, M. & Thonke, K. Polarization fields of III-nitrides grown in different crystal orientations. *J. Phys. Condens. Matter* **19**, 403201 (2007).
- Park, S.-H. & Ahn, D. Crystal orientation effects on electronic and optical properties of wurtzite  $\text{ZnO}/\text{MgZnO}$  quantum well lasers. *Opt. Quant. Electron.* **38**, 935–952 (2006).
- Ohtomo, A. & Hwang, H. Y. A high-mobility electron gas at the  $\text{LaAlO}_3/\text{SrTiO}_3$  heterointerface. *Nature* **427**, 423–426 (2004).
- Ohtomo, A., Müller, D. A., Grazul, J. L. & Hwang, H. Y. Artificial charge-modulation in atomic-scale perovskite titanate superlattices. *Nature* **419**, 378–380 (2002).
- Jang, H. W. *et al.* Metallic and insulating oxide interfaces controlled by electronic correlations. *Science* **331**, 886–889 (2011).
- Biscaras, J. *et al.* Two-dimensional superconductivity at a Mott insulator/band insulator interface  $\text{LaTiO}_3/\text{SrTiO}_3$ . *Nat. Commun.* **1**, 89 (2010).
- Hotta, Y., Susaki, T. & Hwang, H. Y. Polar discontinuity doping of the  $\text{LaVO}_3/\text{SrTiO}_3$  interface. *Phys. Rev. Lett.* **99**, 236805 (2007).
- Perna, P. *et al.* Conducting interfaces between band insulating oxides: The  $\text{LaGaO}_3/\text{SrTiO}_3$  heterostructure. *Appl. Phys. Lett.* **97**, 152111 (2010).
- Moetakef, P. *et al.* Transport in ferromagnetic  $\text{GdTiO}_3/\text{SrTiO}_3$  heterostructures. *Appl. Phys. Lett.* **98**, 112110 (2011).
- Chen, Y. Z. *et al.* A high-mobility two-dimensional electron gas at the spinel/perovskite interface of  $\gamma\text{-Al}_2\text{O}_3/\text{SrTiO}_3$ . *Nat. Commun.* **4**, 1371 (2013).
- Ueno, K. *et al.* Discovery of superconductivity in  $\text{KTaO}_3$  by electrostatic carrier doping. *Nat. Nanotechnol.* **6**, 408–412 (2011).
- Kozuka, Y. *et al.* Two-dimensional normal-state quantum oscillations in a superconducting heterostructures. *Nature* **462**, 487–490 (2009).
- Reyren, N. *et al.* Superconducting interfaces between insulating oxides. *Science* **317**, 1196–1199 (2007).
- Caviglia, A. D. *et al.* Electric field control of the  $\text{LaAlO}_3/\text{SrTiO}_3$  interface ground state. *Nature* **456**, 624–637 (2008).
- Biscaras, J. *et al.* Two-dimensional superconducting phase in  $\text{LaTiO}_3/\text{SrTiO}_3$  heterostructures induced by high-mobility carrier doping. *Phys. Rev. Lett.* **108**, 247004 (2012).
- Gardner, H. J. *et al.* Enhancement of superconductivity by a parallel magnetic field in two-dimensional superconductors. *Nat. Phys.* **7**, 895–900 (2011).
- Kim, M., Kozuka, Y., Bell, C., Hikita, Y. & Hwang, H. Y. Intrinsic spin-orbit coupling in superconducting  $\delta$ -doped  $\text{SrTiO}_3$  heterostructures. *Phys. Rev. B* **86**, 085121 (2012).

19. Schneider, T., Caviglia, A. D., Gariglio, S., Reyren, N. & Triscone, J.-M. Electrostatically-tuned superconductor-metal-insulator quantum transition at the  $\text{LaAlO}_3/\text{SrTiO}_3$  interface. *Phys. Rev. B* **79**, 184502 (2009).
20. Biscaras, J. *et al.* Multiple quantum criticality in a two-dimensional superconductor. *Nat. Mater.* **12**, 542–548 (2013).
21. Warusawithana, M. P. *et al.*  $\text{LaAlO}_3$  stoichiometry is key to electron liquid formation at  $\text{LaAlO}_3/\text{SrTiO}_3$  interfaces. *Nat. Commun.* **4**, 2351 (2013).
22. Herranz, G., Sánchez, F., Dix, N., Scigaj, M. & Fontcuberta, J. High mobility conduction at (110) and (111)  $\text{LaAlO}_3/\text{SrTiO}_3$  interfaces. *Sci. Rep.* **2**, 758 (2012).
23. Annadi, A. *et al.* Anisotropic two-dimensional electron gas at the  $\text{LaAlO}_3/\text{SrTiO}_3$  (110) interface. *Nat. Commun.* **4**, 1838 (2013).
24. Pesquera, D. *et al.* Two-Dimensional electron gases at  $\text{LaAlO}_3/\text{SrTiO}_3$  interfaces: orbital symmetry and hierarchy engineered by crystal orientation. *Phys. Rev. Lett.* **113**, 156802 (2014).
25. Wang, Z. *et al.* Anisotropic two-dimensional electron gas at  $\text{SrTiO}_3$ (110). *Proc. Natl Acad. Sci.* **111**, 3933 (2014).
26. Bachelet, R., Valle, F., Infante, I., Sánchez, F. & Fontcuberta, J. Step formation, faceting, and bunching in atomically flat (110) surfaces. *Appl. Phys. Lett.* **91**, 251904 (2007).
27. Sánchez, F., Ocal, C. & Fontcuberta, J. Tailored surfaces of perovskite oxide substrates for conducted growth of thin films. *Chem. Soc. Rev.* **43**, 2272–2285 (2014).
28. Pennycook, S. J. & Nellist, P. D. *Scanning Transmission Electron Microscopy* (Springer, 2011).
29. Bando, H., Aiura, Y., Haruyama, Y., Shimizu, T. & Nishihara, Y. Structure and electronic states on reduced  $\text{SrTiO}_3$ (110) surface observed by scanning tunneling microscopy and spectroscopy. *J. Vac. Sci. Technol. B* **13**, 1150–1154 (1995).
30. Bottin, F., Finocchi, F. & Noguera, C. Facetting and  $(n \times 1)$  reconstructions of  $\text{SrTiO}_3$ (1 1 0) surfaces. *Surf. Sci.* **574**, 65–76 (2005).
31. Tinkham, M. *Introduction to Superconductivity* 2nd ed. (Dover, 1996).
32. Kosterlitz, J. M. & Thouless, D. J. Ordering, metastability and phase transitions in two-dimensional systems. *J. Phys. C Solid State Phys.* **6**, 1181–1203 (1973).
33. Beasley, M. R., Mooij, J. E. & Orlando, T. P. Possibility of vortex-antivortex pair dissociation in two-dimensional superconductors. *Phys. Rev. Lett.* **42**, 1165–1168 (1979).
34. She, J.-H. & Balatsky, A. V. Berezinskii-Kosterlitz-Thouless transition to the superconducting state of heavy-fermion superlattices. *Phys. Rev. Lett.* **109**, 077002 (2012).
35. Reyren, N. *et al.* Anisotropy of the superconducting transport properties of the  $\text{LaAlO}_3/\text{SrTiO}_3$  interface. *Appl. Phys. Lett.* **94**, 112506 (2009).
36. Chandrasekhar, B. S. A note on the maximum critical field of high-field superconductors. *Appl. Phys. Lett.* **1**, 7 (1962).
37. Kim, J. S. *et al.* Nonlinear Hall effect and multichannel conduction in  $\text{LaTiO}_3/\text{SrTiO}_3$  superlattices. *Phys. Rev. B* **82**, 201407 (2010).
38. Caviglia, A. D. *et al.* Tunable Rashba spin-orbit interaction at oxide interfaces. *Phys. Rev. Lett.* **104**, 126803 (2010).
39. Ben Shalom, M., Sachs, M., Rakhmilevitch, D., Palevski, A. & Dagan, Y. Tuning spin-orbit coupling and superconductivity at the  $\text{SrTiO}_3/\text{LaAlO}_3$  interface: a magnetotransport study. *Phys. Rev. Lett.* **104**, 126802 (2010).
40. Khalsa, G., Lee, B. & MacDonald, A. H. Y. Theory of  $t_{2g}$  electron-gas Rashba interactions. *Phys. Rev. B* **88**, 041302(R) (2013).
41. Shanavas, K. V. & Satpathy, S. Electric field tuning of the Rashba effect in the polar perovskite structures. *Phys. Rev. Lett.* **112**, 086802 (2014).
42. Maekawa, S. & Fukuyama, H. Magnetoresistance in two-dimensional disordered systems: effects of Zeeman splitting and spin-orbit scattering. *J. Phys. Soc. Jpn* **50**, 2516–2524 (1981).
43. Fête, A., Gariglio, S., Caviglia, A. D., Triscone, J.-M. & Gabay, M. Rashba induced magnetoconductance oscillations in the  $\text{LaAlO}_3$ - $\text{SrTiO}_3$  heterostructure. *Phys. Rev. B* **86**, 201105(R) (2012).
44. Reyren, N. *et al.* Gate-controlled spin injection at  $\text{LaAlO}_3/\text{SrTiO}_3$  interfaces. *Phys. Rev. Lett.* **108**, 186802 (2012).
45. Santander-Syro, A. F. *et al.* Giant spin splitting of the two-dimensional electron gas at the surface of  $\text{SrTiO}_3$ . *Nat. Mater.* **13**, 1085–1090 (2014).
46. Santander-Syro, A. F. *et al.* Two-dimensional electron gas with universal subbands at the surface of  $\text{SrTiO}_3$ . *Nature* **469**, 189–193 (2011).
47. Son, W.-J., Cho, E., Lee, B., Lee, J. & Han, S. Density and spatial distribution of charge carriers in the intrinsic n-type  $\text{LaAlO}_3$ - $\text{SrTiO}_3$  interface. *Phys. Rev. B* **79**, 245411 (2009).
48. Berner, G. *et al.* Direct k-Space mapping of the electronic structure in an oxide-oxide interface. *Phys. Rev. Lett.* **110**, 247601 (2013).
49. Salluzzo, M. *et al.* Orbital reconstruction and the two-dimensional electron gas at the  $\text{LaAlO}_3/\text{SrTiO}_3$  interface. *Phys. Rev. Lett.* **102**, 166804 (2009).
50. Koster, G., Boike, L. K., Rijnders, G. J. H. M., Blank, D. H. A. & Rogalla, H. Quasi-ideal strontium titanate crystal surfaces through formation of strontium hydroxide. *Appl. Phys. Lett.* **73**, 2920–2922 (1998).
51. Kawasaki, M. *et al.* Atomic control of the  $\text{SrTiO}_3$  crystal surface. *Science* **266**, 1540–1542 (1994).

## Acknowledgements

This work was supported by the Spanish MAT2011-29269-C03 project, the RyC-2012-11709 contract of J.G. and the Generalitat de Catalunya (2014 SGR 734 project) and by the Region Île-de-France in the frame-work of CNano IdF programme. The HRTEM microscopy work was in part conducted in the ‘Laboratorio de Microscopías Avanzadas’ at the Instituto de Nanociencia de Aragón-Universidad de Zaragoza. We acknowledge the LMA-INA for offering access to their instruments. J.G. is grateful to Dr A. Ibarra for the help at LMA-INA. Electron microscopy observations at ORNL were supported by the U.S. Department of Energy (DOE), Basic Energy Sciences (BES), Materials Sciences and Engineering Division.

## Author contributions

G.H. designed and conceived the experiments with help from J.F., N.B. and J.L. Low-temperature magnetotransport experiments were done by G.S., A.J. and N.B. The analysis of low-temperature magnetotransport data was done by G.S., N.B. and G.H. The thin film preparation, *in situ* reflection high-energy electron diffraction characterization and structural and surface morphology analysis were done by M.S., N.D. and F.S. J.G., and M.V. made all the characterization and analysis of structural characterization by STEM-HAADF. G.H. wrote the paper. All authors discussed the data and commented on the paper.

## Additional information

**Supplementary Information** accompanies this paper at <http://www.nature.com/naturecommunications>

**Competing financial interests:** The authors declare no competing financial interests.

**Reprints and permission** information is available online at <http://npg.nature.com/reprintsandpermissions/>

**How to cite this article:** Herranz, G. *et al.* Engineering two-dimensional superconductivity and Rashba spin-orbit coupling in  $\text{LaAlO}_3/\text{SrTiO}_3$  quantum wells by selective orbital occupancy. *Nat. Commun.* **6**:6028 doi: 10.1038/ncomms7028 (2015).



This work is licensed under a Creative Commons Attribution 4.0 International License. The images or other third party material in this article are included in the article's Creative Commons license, unless indicated otherwise in the credit line; if the material is not included under the Creative Commons license, users will need to obtain permission from the license holder to reproduce the material. To view a copy of this license, visit <http://creativecommons.org/licenses/by/4.0/>